



CHORUS

This is the accepted manuscript made available via CHORUS. The article has been published as:

Two-body transient viscous interactions in free space

Bo Liu and Sukalyan Bhattacharya

Phys. Rev. Fluids **6**, 104305 — Published 19 October 2021

DOI: [10.1103/PhysRevFluids.6.104305](https://doi.org/10.1103/PhysRevFluids.6.104305)

Two-body Transient Viscous Interactions in Free Space

Bo Liu* and Sukalyan Bhattacharya

Department of Mechanical Engineering,

Texas Tech University,

Lubbock, Texas 79409, USA

(Dated: September 24, 2021)

Abstract

This article elucidates how unsteady hydrodynamic interactions between two closely situated spheres in viscous liquid affect their time-dependent motion. The system represents typical Brownian particles for which temporal inertia is always comparable to the viscous forces even though convective inertia is negligible. The analysis quantifies the transient mutual interactions in terms of frequency-dependent friction coefficients of both spheres as well as their temporally varying mobility response to an impulsive force. To this end, a new generalization of Stokesian dynamics is formulated, where instead of Stokes equation, linearized unsteady Navier-Stokes is Fourier transformed in frequency space to describe flow fields. Accordingly, two complete sets of basis functions for Brinkman equation instead of Stokes equation are constructed in spherical co-ordinates centered around two particles. The mutual transformations between these two sets enable the enforcement of the no-slip boundary conditions on all solid-liquid interfaces. The resulting algebraic relations provide the frequency-dependent two-body frictions, whereas inverse Fourier transform of these after adding appropriate inertial contributions yield time-dependent mobility response. The friction and mobility values are validated in limiting cases under short-time and long-time limits. The scaling laws of these quantities are also explored as functions of the separation distance between two solid bodies revealing important physical insight into the complicated dynamics.

I. INTRODUCTION

Mutual hydrodynamic interactions between particles suspended in a viscous fluid are crucially important in colloidal dynamics and particle transport mechanisms. For example, such effect dictates whether attracting solid species can overcome fluid-induced stretching to form clusters in shear flow [1, 2]. Similarly, these interactions affect particulate motions causing increase in diffusivity [3, 4], modification in solute concentration [5, 6] and change in separation patterns [5, 7–11]. Especially in dense suspensions, influence of one particle on others plays a crucial role in rheological estimations [12, 13]. In nano-fluids, this also impacts thermal dynamics by altering Brownian motion as force on one submicron body not only instigates its motion but also induces flow moving others [14, 15].

* Department of Mechanical Engineering, Texas Tech University, Lubbock, Texas 79409, USA

For the aforementioned reasons, many past investigations have focused on the analysis of mutual interparticle hydrodynamic interactions inside viscous fluid. Typically these studies have considered quasi-steady dynamics where the time-scales for temporal variations are assumed to be much larger than the viscous time-scale. As a result, the methods have been developed to solve steady linearized viscous flow equations, and the resulting plethora of works are grouped as Stokesian dynamics analysis. Numerous articles over past few decades have ultimately made this field matured [16–22].

The underlying quasi-steady assumption in Stokesian dynamics is, however, not true often. For example, if suspended particles encounter high frequency but low amplitude shearing oscillation, the flow interactions should be governed by linearized but unsteady equation. The reason is: while small amplitude allows linearization due to negligible convection, high frequency makes the problem unsteady by ensuring comparable temporal and viscous time-scales. More importantly, such similarity between two scales are always true in Brownian dynamics. This happens because after being instigated by a random force a Brownian particle decelerates solely due to viscous resistance making the duration of transiency and momentum diffusion exactly same. Thus, a proper analysis of Brownian effect can only be achieved if quasi-steady Stokesian dynamics can be extended to include unsteadiness. This is especially true for many-body dynamics where product of Reynolds and Strouhal numbers is of the order of unity, and interparticle distance is within a few particulate diameters. A typical moderately dense Brownian system satisfies these conditions. This is why all contemporary Brownian theories include the effect of transient inertia [23, 24].

A general numerical methodology to describe such unsteady problems is gathering increasing relevance in contemporary research. Recently, suspensions of nano-spheres are shown to have enhanced thermal conductivity on which the solid solutes with small volume fraction seem to have disproportional impact [14, 15]. The effect can be attributed to Brownian motion where nano-particles drag fluid during their random motion acting as multiple stirrers causing increased heat transfer. This phenomenon can only be analyzed by many-body unsteady Brownian interactions quantifying their cumulative contributions. Similarly, recent predictions based on micro-rheology depend on recording time-dependent random motion of submicron tracers so that viscoelastic properties can be estimated from the data [12, 13]. This is especially useful for fragile samples which cannot withstand the stresses in a conventional rheometers during the measurement process. Analysis of unsteady mutual

interactions between neighboring particles can improve the micro-rheological technology by eliminating the error induced by neighboring tracers in a multiple tracing system. This can be beneficial in two different ways for microrheology. Firstly, if closely situated multiple bodies are tracked with proper interaction estimation, the observation time to acquire same amount of data can be shorten making the detection faster. Secondly, the correction can rectify the errors in simulations with periodic grids by quantifying the effect of neighboring cells.

Some past articles have considered unsteady dynamics among many bodies to address the aforementioned problems. These works include analysis of subdominant inertia [25], externally imposed unsteadiness [26] and inter-particulate hydrodynamic interactions [27, 28]. Our present manuscript is, however, substantially different from these earlier papers.

This article addresses the necessity of unsteady many-body simulation by generalizing the basic mathematical procedure for Stokesian dynamics. The entire formulation consists of four major steps. Firstly, the linearized unsteady flow equation is transformed from temporal to frequency domain, and the time-invariant fields in Fourier space is constructed as spatial functions. Then, the resulting governing relation for spatial variations in the form of temporally invariant but spatially dependent Brinkman equation is solved in presence of disconnected particles using appropriate basis functions. Thirdly, a set of algebraic relations involving unknown amplitudes of basis functions is constructed by exploiting given boundary conditions yielding frequency-dependent many-body friction coefficients. Finally, these frictions are inserted in equation of motion to find the unsteady mobility response of all suspended bodies to an impulsive force or torque on any of these. The first two of these components are extensively discussed and validated in our earlier work [29] which presents detailed solutions of Brinkman equation under various conditions. The current study builds on it by completing the last two steps required for simulating unsteady many-body motion.

The outlined analysis facilitates a hitherto unrealized study of two-body unsteady flow interactions. In the past, there have been investigations on time-dependent motion of a single particle. Some earlier works have also focused on solving Brinkman equation in the context of flow in porous medium. To best of our knowledge, the fundamental simulation of multiparticle unsteady motion, however, has not been undertaken yet.

Consequently, this paper renders two very important results. Firstly, it provides the frequency-dependent general frictions for a two-sphere system including both self and mutual

coefficients. Secondly, it shows how the motion of both varies with time if any one of these is impacted by an impulsive force or torque. The friction results are validated with known Stokesian values for different inter-particle separations under low frequency or long-time limit. In contrast, the unsteady mobility response is verified in ballistic regime under short-time limit. Such dual validations under two opposite limits confirm the accuracy of our analysis.

Accordingly, this paper is organized in the following way. In section 2, we outline the relevant details of the basis function expansion and the subsequent mathematical formulation to find the frictions. Section 3 presents all non-trivial friction coefficients for two-sphere system as function of frequency for different inter-particle separations. The corresponding unsteady mobility responses are shown in section 4 as functions of time. Finally, the article is summarized, and the conclusions are drawn in section 5.

II. GENERAL SOLUTION AND MATRIX FORMULATION

This paper considers unsteady flow around two spheres of radius a with center-to-center distance s . A fluid with viscosity μ and density ρ surrounds the particles, and freely extends to infinity. The liquid remains quiescent far away from the moving spheres.

The velocity in the domain is induced by force or torque on either of the spheres. These are driven in such a way that the time-scale of fluctuations in the fields is comparable to momentum diffusion. On the other hand, the instigation behind the motion is mild enough to create a small velocity scale so that the non-linear convective contribution can be neglected. Under such conditions, the hydrodynamic fields in such system are governed by linearized unsteady Navier-Stokes equation:

$$\frac{\partial \mathbf{v}}{\partial t} = -\nabla p + \nabla^2 \mathbf{v}, \quad \nabla \cdot \mathbf{v} = 0. \quad (1)$$

Here, \mathbf{v} is the non-dimensional velocity normalized by scale v_s , and p is the non-dimensional pressure normalized by $\mu v_s/a$. Also, dimensionless time t and space \mathbf{r} are normalized by viscous temporal scale $a^2 \rho/\mu$ and characteristic geometric dimension a , respectively.

The unsteady equation in eq.1 is complemented by the boundary conditions at the infinity and at the surface of the spheres. In our problem, we consider all hydrodynamic fields to decay far away from the particles. Also, the solid-liquid interfaces are assumed to be no-slip

so that the fluid at the contact assumes the velocity corresponding to the translation and rotation of the spheres.

A. Time-invariant decomposition in Fourier space

Fourier variation $\exp(i\Omega t)$ is the eigen function for the temporal derivative in eq.1. It involves non-dimensional frequency Ω which is normalized by inverse of viscous time-scale to form dimensionless spectral space. A Fourier transform in such space help us to create time-invariant fields only dependent on spatial co-ordinates.

Accordingly, we expand the hydrodynamic fields in Fourier space:

$$\mathbf{v}(\mathbf{r}, t) = \int_{-\infty}^{\infty} \mathbf{v}_{\Omega}(\mathbf{r}) \exp(i\Omega t) d\Omega, \quad p(\mathbf{r}, t) = \int_{-\infty}^{\infty} p_{\Omega}(\mathbf{r}) \exp(i\Omega t) d\Omega. \quad (2)$$

The time-independent $\mathbf{v}_{\Omega}(\mathbf{r})$ and $p_{\Omega}(\mathbf{r})$ are constructed by inverse Fourier transform:

$$\mathbf{v}_{\Omega}(\mathbf{r}) = \frac{1}{2\pi} \int_{-\infty}^{\infty} \mathbf{v}(\mathbf{r}, t) \exp(-i\Omega t) dt, \quad p_{\Omega}(\mathbf{r}) = \frac{1}{2\pi} \int_{-\infty}^{\infty} p(\mathbf{r}, t) \exp(-i\Omega t) dt, \quad (3)$$

as per the orthogonality relations for sinusoidal functions.

Our strategy is to solve for $\mathbf{v}_{\Omega}(\mathbf{r})$ and $p_{\Omega}(\mathbf{r})$ enforcing both interfacial no-slip and far-field decay conditions. Combining eqs.2 and 1, one infers that \mathbf{v}_{Ω} and p_{Ω} satisfy:

$$i\Omega \mathbf{v}_{\Omega} = -\nabla p_{\Omega} + \nabla^2 \mathbf{v}_{\Omega}, \quad \nabla \cdot \mathbf{v}_{\Omega} = 0. \quad (4)$$

This is generalized Brinkman equation with complex constant in the form of $i\Omega$ in the left hand side of the momentum equation. We apply our recently developed solution techniques [29] for such equations to find \mathbf{v}_{Ω} and p_{Ω} around the two particles of interest.

B. Brief outline of the solution techniques for Brinkman equation

Vector field solution for Brinkman equation in presence of two disconnected spheres is described in our recent article [29]. First, we expand the field solution for eq.4 in terms of two complete sets of basis functions in two spherical coordinates centered around the respective two particles. Then, the transformation coefficients are derived to convert the representation of the flow in one set to the other. This leads to a system of algebraic relations coupling the unknown amplitudes to the given boundary conditions. Finally, the spectrally converged

values of unknown amplitudes can be obtained by inverting the matrix representing the algebraic equations with adequate number of basis functions. Our earlier work validated the aforementioned mathematical theory using detailed simulations. This solution technique also applies to the unsteady motion of two particles in an infinitely extended viscous liquid where the eigen constant considered in Brinkman relation is imaginary.

Following the outlined procedure, we express the time-independent field \mathbf{v}_Ω in eq.4:

$$\mathbf{v}_\Omega = \sum_{lms} (\alpha_{lms}^{1-} \mathbf{v}_{lms}^{1-} + \alpha_{lms}^{2-} \mathbf{v}_{lms}^{2-}) \quad (5)$$

as a linear combination of vectorially separable basis functions $\mathbf{v}_{lms}^{i\pm}$. The superscript i in $\mathbf{v}_{lms}^{i\pm}$ means that $\mathbf{v}_{lms}^{i\pm}$ are the function of the spherical coordinates centered around the point $\mathbf{r} = \mathbf{x}_i$ which is the location of the center of the i -th particle. The translational invariance of Brinkman relation ensures

$$\mathbf{v}_{lms}^{i\pm} = \mathbf{v}_{lms}^{\pm}(\mathbf{r} - \mathbf{x}_i). \quad (6)$$

The extra superscript $+$ represents regular solutions which are finite at the origin of the local coordinate, but diverge at infinity. In contrast, the “ $-$ ” stands for singular functions with singularity at the origin and vanishing strength far away. For unbounded fluid, regular solutions are not present in eq.5 for their unphysical infinite value at infinity. The subscripts l and m are associated to the complete set of scalar spherical harmonic functions Y_{lm} . These can be interpreted as respective quantum numbers in θ and ϕ directions for $r-\theta-\phi$ spherical coordinate system with $l=1,2,3,\dots$ and $m=0,\pm 1,\pm 2,\dots,\pm l$. The subscript $s=1,2,3$ denotes three independent vectors to ensure the completeness of basis solutions in three dimensional space. These are similar to Lamb’s solutions for Steady Stokes equation in the spherical coordinate. We derive them as

$$\mathbf{v}_{lm1}^{\pm}(\mathbf{r}_i) = \mathbf{r}_i \times \nabla \psi_{lm}^{\text{h}\pm}(\mathbf{r}_i), \quad \mathbf{v}_{lm2}^{\pm}(\mathbf{r}_i) = \nabla \times \mathbf{v}_{lm1}^{\pm}(\mathbf{r}_i), \quad \mathbf{v}_{lm3}^{\pm}(\mathbf{r}_i) = \frac{i}{\Omega} \nabla \psi_{lm}^{\text{PI}\pm}(\mathbf{r}_i), \quad (7)$$

where $\mathbf{r}_i = \mathbf{r} - \mathbf{x}_i$, and

$$\psi_{lm}^{\text{PI}+}(\mathbf{r}_i) = r_i^l Y_{lm}^i, \quad \psi_{lm}^{\text{PI}-}(\mathbf{r}_i) = r_i^{-l-1} Y_{lm}^i, \quad \psi_{lm}^{\text{h}+}(\mathbf{r}_i) = \frac{g_l^+(r_i)}{r_i} Y_{lm}^i, \quad \psi_{lm}^{\text{h}-}(\mathbf{r}_i) = \frac{g_l^-(r_i)}{r_i} Y_{lm}^i \quad (8)$$

with i indicating quantities corresponding to the i -th particle. So variables r_i, θ_i, ϕ_i are three spherical coordinates with the point $\mathbf{r}_i = \mathbf{x}_i$ as the center. The functions g_l^{\pm} can be found from the subsequent recurrence relation

$$g_l^{\pm}(r_i) = \left(\frac{d}{dr_i} - \frac{l}{r_i} \right) g_{l-1}^{\pm}(r_i) \quad (9)$$

and the initial ones are represented by:

$$g_0^+(r_i) = \sinh(kr_i), \quad g_0^-(r_i) = \exp(-kr_i), \quad (10)$$

where $k = \frac{\sqrt{2\Omega}}{2}(1 + i)$. After all basis functions $\mathbf{v}_{lms}^{i\pm}$ are constructed, field solution \mathbf{v}_Ω would be completely obtained if we evaluate unknown amplitudes α_{lms}^{i-} in eq.5. Thus, we concentrate on finding these by applying the given boundary conditions.

C. Matrix formulation for unknown amplitudes

The unknown amplitudes α_{lms}^{i-} are obtained from the boundary conditions by constructing a set of algebraic relations in matrix form. The construction of these matrices is a three-step process.

Firstly, we recognize any vector function on the surface of the i -th particle can be expanded in terms of the following interfacial basis involving spherical harmonics:

$$\hat{\mathbf{e}}_{lm1}^i = \mathbf{r}_i \times \nabla Y_{lm}^i, \quad \hat{\mathbf{e}}_{lm2}^i = \hat{\mathbf{e}}_{r_i} Y_{lm}^i, \quad \hat{\mathbf{e}}_{lm3}^i = r_i \nabla Y_{lm}^i. \quad (11)$$

Thus, the given velocity $\mathbf{v}_i(\theta_i, \phi_i)$ on the surface of the i -th sphere can be expanded as:

$$\mathbf{v}_i(\theta_i, \phi_i) = \sum_{lm\sigma} [a_{lm\sigma}^i \hat{\mathbf{e}}_{lm\sigma}^i(\theta_i, \phi_i)], \quad (12)$$

where $a_{lm\sigma}^i$ are known constants because \mathbf{v}_i is provided. Likewise, the basis functions $\mathbf{v}_{lms}^{i\pm}$ can also be expanded as combination of $\hat{\mathbf{e}}_{lm\sigma}^i$:

$$\mathbf{v}_{lms}^{i\pm} = \sum_{\sigma} [f_{lms\sigma}^{\pm}(r_i) \hat{\mathbf{e}}_{lm\sigma}^i(\theta_i, \phi_i)]. \quad (13)$$

Here, the scalar functions $f_{lms\sigma}^{\pm}$ depend only on r_i making these invariant of angular coordinates. These functions are constructed from the following relations

$$\begin{aligned} \mathbf{v}_{lm1}^{i\pm} &= \frac{g_l^{\pm}(r_i)}{r_i} \hat{\mathbf{e}}_{lm1}^i, & \mathbf{v}_{lm2}^{i\pm} &= -\frac{l(l+1)}{r_i^2} g_l^{\pm}(r_i) \hat{\mathbf{e}}_{lm2}^i - \frac{g_l^{\pm'}(r_i)}{r_i} \hat{\mathbf{e}}_{lm3}^i, \\ \mathbf{v}_{lm3}^{i+} &= l r_i^{l-1} \hat{\mathbf{e}}_{lm2}^i + r_i^{l-1} \hat{\mathbf{e}}_{lm3}^i, & \mathbf{v}_{lm3}^{i-} &= (-l-1) r_i^{-l-2} \hat{\mathbf{e}}_{lm2}^i + r_i^{-l-2} \hat{\mathbf{e}}_{lm3}^i. \end{aligned} \quad (14)$$

We realize that it is convenient to use a 3×3 matrix representation $[\mathbf{F}_{lm}^{\pm}]$

$$[\mathbf{F}_{lm}^+] = \begin{bmatrix} \frac{g_l^+(r_i)}{r_i} & 0 & 0 \\ 0 & -\frac{l(l+1)}{r_i^2} g_l^+(r_i) & -\frac{g_l^{+'}(r_i)}{r_i} \\ 0 & l r_i^{l-1} & r_i^{l-1} \end{bmatrix}, \quad [\mathbf{F}_{lm}^-] = \begin{bmatrix} \frac{g_l^-(r_i)}{r_i} & 0 & 0 \\ 0 & -\frac{l(l+1)}{r_i^2} g_l^-(r_i) & -\frac{g_l^{-'}(r_i)}{r_i} \\ 0 & (-l-1) r_i^{-l-2} & r_i^{-l-2} \end{bmatrix} \quad (15)$$

with $f_{lms\sigma}^\pm$ being the σ -th element of the s -th row in $[F_{lm}^\pm]$.

Secondly, we derive a transformation matrix $[M_{ij}^\mp]$ which relates the two sets of basis vectors \mathbf{v}_{lms}^{i-} and \mathbf{v}_{lms}^{j+}

$$\mathbf{v}_{lms}^{i-} = \sum_{l'm's'} M_{lmsl'm's'}^{ij\mp} \mathbf{v}_{l'm's'}^{j+} \quad (16)$$

for $|\mathbf{r} - \mathbf{x}_j| < |\mathbf{x}_i - \mathbf{x}_j|$. As a result, the field solution in eq.5 can be expressed in one single spherical coordinates with origin at the center of either particles. This allows us to build relations between unknown amplitudes α_{lms}^{i-} and given constants a_{lms}^i known from the boundary conditions. As a result, on the surface of the first particle, one finds

$$a_{\lambda\mu\sigma}^1 = \sum_s [\alpha_{\lambda\mu s}^{1-} f_{\lambda\mu\sigma}^-(a_1)] + \sum_{lms s'} [\alpha_{lms}^{2-} M_{lms\lambda\mu s'}^{21\mp} f_{\lambda\mu s'\sigma}^+(a_1)]. \quad (17)$$

Similarly, boundary condition around the second particle implies

$$a_{\lambda\mu\sigma}^2 = \sum_s [\alpha_{\lambda\mu s}^{2-} f_{\lambda\mu\sigma}^-(a_2)] + \sum_{lms s'} [\alpha_{lms}^{1-} M_{lms\lambda\mu s'}^{12\mp} f_{\lambda\mu s'\sigma}^+(a_2)], \quad (18)$$

where a_i in parentheses means radius of the i -th particle.

Finally, a matrix relation

$$\langle \mathbf{a} | = \langle \alpha | [\mathbf{G}] \quad (19)$$

is formed by combining eqs. 17 and 18. Here, both $\langle \mathbf{a} |$ and $\langle \alpha |$ are row matrices containing elements $a_{\lambda\mu\sigma}^1$, $a_{\lambda\mu\sigma}^2$ and α_{lms}^{1-} , α_{lms}^{2-} , respectively. The amplitudes for both particles are stacked together so that the respective subsets are displayed as sub-rows

$$\langle \mathbf{a} | = \langle \{a_{\lambda\mu\sigma}^1\}, \{a_{\lambda\mu\sigma}^2\} |, \quad \langle \alpha | = \langle \{\alpha_{lms}^{1-}\}, \{\alpha_{lms}^{2-}\} |. \quad (20)$$

The square matrix $[\mathbf{G}]$ is the grand mobility matrix with the following sub-structures

$$[\mathbf{G}] = \begin{bmatrix} [F_1^-] & [M_{12}^\mp][F_2^+] \\ [M_{21}^\mp][F_1^+] & [F_2^-] \end{bmatrix}, \quad (21)$$

where both $[F_i^\pm]$ and $[M_{ij}^\mp]$ are square sub-matrices. Thus, as row matrix $\langle \mathbf{a} |$ conveying boundary conditions is given, unknown amplitudes $\langle \alpha |$ are evaluated by inverting grand mobility $[\mathbf{G}]$ and post-multiplying the inverse with $\langle \mathbf{a} |$. Then, one can compute first \mathbf{v}_Ω from eq.5 and subsequently \mathbf{v} using eq.2. Thus, the computation of the hydrodynamic fields will be possible in an accurate and efficient way.

III. FREQUENCY DEPENDENT FRICTION TENSOR

This section focuses on finding the hydrodynamic force and torque on each particle in frequency space Ω for given rectilinear and rotational motion. Accordingly, we define linear $\mathbf{u}_i(t)$ and angular $\boldsymbol{\omega}_i(t)$ velocities for the i -th sphere as time-dependent vectors. Similarly, the force and torque acting on it are denoted as $\mathbf{f}_i(t)$ and $\boldsymbol{\tau}_i(t)$ as temporal functions, respectively. All these unsteady quantities are expanded as Fourier transforms:

$$\mathbf{u}_i(t) = \int_{-\infty}^{\infty} \hat{\mathbf{u}}_i(\Omega) \exp(i\Omega t) d\Omega, \quad \boldsymbol{\omega}_i(t) = \int_{-\infty}^{\infty} \hat{\boldsymbol{\omega}}_i(\Omega) \exp(i\Omega t) d\Omega, \quad (22)$$

and

$$\mathbf{f}_i(t) = \int_{-\infty}^{\infty} \hat{\mathbf{f}}_i(\Omega) \exp(i\Omega t) d\Omega, \quad \boldsymbol{\tau}_i(t) = \int_{-\infty}^{\infty} \hat{\boldsymbol{\tau}}_i(\Omega) \exp(i\Omega t) d\Omega. \quad (23)$$

Here, the following inverse Fourier transforms are used

$$\hat{\mathbf{u}}_i(\Omega) = \frac{1}{2\pi} \int_{-\infty}^{\infty} \mathbf{u}_i(t) \exp(-i\Omega t) dt, \quad \hat{\boldsymbol{\omega}}_i(\Omega) = \frac{1}{2\pi} \int_{-\infty}^{\infty} \boldsymbol{\omega}_i(t) \exp(-i\Omega t) dt, \quad (24)$$

and

$$\hat{\mathbf{f}}_i(\Omega) = \frac{1}{2\pi} \int_{-\infty}^{\infty} \mathbf{f}_i(t) \exp(-i\Omega t) dt, \quad \hat{\boldsymbol{\tau}}_i(\Omega) = \frac{1}{2\pi} \int_{-\infty}^{\infty} \boldsymbol{\tau}_i(t) \exp(-i\Omega t) dt \quad (25)$$

to reveal translation, rotation, force and torque for the i -th body in the frequency space.

The linearized governing equation allows superposition of solutions corresponding to individual components of the rigid body motion. Thus, friction tensors can be constructed relating the force and torque on the pair of particles to their linear and angular velocities. Such frequency-dependent second order friction tensors $\hat{\mathbf{J}}_{ij}^{tt}(\Omega)$, $\hat{\mathbf{J}}_{ij}^{tr}(\Omega)$, $\hat{\mathbf{J}}_{ij}^{rt}(\Omega)$, $\hat{\mathbf{J}}_{ij}^{rr}(\Omega)$ are defined to express $\hat{\mathbf{f}}_i(\Omega)$ and $\hat{\boldsymbol{\tau}}_i(\Omega)$ in terms of $\hat{\mathbf{u}}_j(\Omega)$ and $\hat{\boldsymbol{\omega}}_j(\Omega)$:

$$\hat{\mathbf{f}}_i(\Omega) = \sum_j [\hat{\mathbf{J}}_{ij}^{tt}(\Omega) \cdot \hat{\mathbf{u}}_j(\Omega) + \hat{\mathbf{J}}_{ij}^{tr}(\Omega) \cdot \hat{\boldsymbol{\omega}}_j(\Omega)], \quad \hat{\boldsymbol{\tau}}_i(\Omega) = \sum_j [\hat{\mathbf{J}}_{ij}^{rt}(\Omega) \cdot \hat{\mathbf{u}}_j(\Omega) + \hat{\mathbf{J}}_{ij}^{rr}(\Omega) \cdot \hat{\boldsymbol{\omega}}_j(\Omega)]. \quad (26)$$

Here, superscripts t and r represent quantities associated to the translational (like $\hat{\mathbf{u}}$, $\hat{\mathbf{f}}$) and rotational (like $\hat{\boldsymbol{\omega}}$, $\hat{\boldsymbol{\tau}}$) vectors. The subscripts i and j in $\hat{\mathbf{J}}_{ij}^{PQ}$ (P, Q denotes t or r) mean the effect on j -th particle generated by motion of the i -th particle. In the non-dimensional formulation, $\hat{\mathbf{J}}_{ij}^{tt}$ and $\hat{\mathbf{J}}_{ij}^{rr}$ are interpreted as frictions normalized by μa and μa^3 , whereas both $\hat{\mathbf{J}}_{ij}^{tr}$ and $\hat{\mathbf{J}}_{ij}^{rt}$ are scaled with μa^2 . It is to be noted that $\hat{\mathbf{J}}_{ij}^{tr}$ is the transpose of $\hat{\mathbf{J}}_{ji}^{rt}$ as per reciprocal theorem. Subscript i in $\hat{\mathbf{f}}_i$ or $\hat{\boldsymbol{\tau}}_i$ stands for force or torque exerted on the i -th particle by the fluid, while subscript j in $\hat{\mathbf{u}}_j(\Omega)$ or $\hat{\boldsymbol{\omega}}_j$ represents linear or angular velocity of the j -th particle.

For two-body system, there are sixteen friction tensors represented by $\widehat{\mathbf{J}}_{ij}^{pq}$ where i or j both can assume the value 1 or 2 independently denoting a specific sphere, and P, Q can stand for either translation or rotation. Our goal is to evaluate all non-trivial elements in these sixteen friction tensors as functions of Fourier frequency Ω . This is realized by using the following contraction, where simple superposition of force and torque from individual basis solution is implemented:

$$\widehat{\mathbf{J}}_{ij}^{PQ} = \sum_{ls\lambda\sigma} \mathbf{v}_{ls}^{(m)P} \cdot \mathbf{G}_{ls\lambda\sigma}^{-1(m)ij} \cdot [\mathbf{w}_{\lambda\sigma}^{(m)Q-} + (\sum_{j\lambda'\sigma'} M_{\lambda\lambda'\sigma\sigma'}^{(m)jk\mp} \cdot \mathbf{w}_{\lambda'\sigma'}^{(m)Q+})]. \quad (27)$$

Here, $\mathbf{v}_{ls}^{(m)P}$ represents the the basis vectors for the given velocity associated to P -type motion as boundary conditions. In contrast, $\mathbf{w}_{\lambda\sigma}^{(m)Q-}$ or $\mathbf{w}_{\lambda'\sigma'}^{(m)Q+}$ means force (if $Q = T$) or torque (if $Q = R$) generated by corresponding singular or regular basis function centered around the respective sphere. Detailed expressions of $\mathbf{v}_{ls}^{(m)P}$, $\mathbf{w}_{\lambda\sigma}^{(m)Q-}$ and $\mathbf{w}_{\lambda'\sigma'}^{(m)Q+}$ are articulated in Appendix A. The corresponding matrix elements in the i -th, j -th block in the inverse of $[\mathbf{G}]$ (see eq.21) are denoted by $\mathbf{G}_{ls\lambda\sigma}^{-1(m)ij}$. Also, $M_{\lambda\lambda'\sigma\sigma'}^{(m)jk\mp}$ are coefficients in a matrix defined as $M_{jk}^{\mp}(1 - \delta_{jk})$ with δ_{jk} being the Kronecker delta.

In eq.27, identical spheres imply that $\widehat{\mathbf{J}}_{11}^{pq} = \widehat{\mathbf{J}}_{22}^{pq}$ as well as $\widehat{\mathbf{J}}_{12}^{pq} = \widehat{\mathbf{J}}_{21}^{pq}$ for $p = q$ and $\widehat{\mathbf{J}}_{12}^{pq} = -\widehat{\mathbf{J}}_{21}^{pq}$ for $p \neq q$. Moreover, reciprocal theorem ensures $\widehat{\mathbf{J}}_{ij}^{pq} = \widehat{\mathbf{J}}_{ji}^{qp\dagger}$ with \dagger being conjugate-transpose. We check that these obvious symmetries are satisfied by eq.27 and the relations in Appendix A. Thus, the non-zero components of the independent tensors are described in the subsequent narration.

A. Validation of friction coefficients with known Stokesian results

We employ eq.27 to calculate independent non-zero elements of $\widehat{\mathbf{J}}_{ij}^{PQ}$, and compare the results with known benchmark values according to Stokesian analysis for $\Omega \rightarrow 0$. Two different separation distances between two spheres are chosen to achieve a comprehensive validation. The comparison is presented in Table 1 which reveals the accuracy of the outlined algorithm emphatically.

The symmetry of the geometry dictates that $\widehat{\mathbf{J}}_{ij}^{tt}$, and $\widehat{\mathbf{J}}_{ij}^{rr}$ are all diagonal tensors. As a result, these can be decomposed into diagonal components:

$$\widehat{\mathbf{J}}_{ij}^{tt} = \widehat{J}_{ij}^{tt\perp} \hat{\mathbf{e}}_z \hat{\mathbf{e}}_z + \widehat{J}_{ij}^{tt\parallel} (\mathbf{I} - \hat{\mathbf{e}}_z \hat{\mathbf{e}}_z) \quad \widehat{\mathbf{J}}_{ij}^{rr} = \widehat{J}_{ij}^{rr\perp} \hat{\mathbf{e}}_z \hat{\mathbf{e}}_z + \widehat{J}_{ij}^{rr\parallel} (\mathbf{I} - \hat{\mathbf{e}}_z \hat{\mathbf{e}}_z). \quad (28)$$

TABLE I. Comparison between Stokesian results and computed Friction values.

	For Separation $s = 2.1$		For Separation $s = 3$	
	Stokesian results	Friction for $\Omega = 10^{-5}$	Stokesian results	Friction for $\Omega = 10^{-5}$
$\widehat{\mathbf{J}}_{11}^{tt}$ Tangential	-26.257	-26.280	-20.280	-20.323
$\widehat{\mathbf{J}}_{11}^{tt}$ Normal	-76.003	-76.018	-25.795	-25.816
$\widehat{\mathbf{J}}_{11}^{rr}$ Tangential	-30.989	-30.990	-25.585	-25.585
$\widehat{\mathbf{J}}_{11}^{rr}$ Normal	-25.844	-25.844	-25.182	-25.182
$\widehat{\mathbf{J}}_{12}^{tt}$ Tangential	12.438	12.416	5.602	5.575
$\widehat{\mathbf{J}}_{12}^{tt}$ Normal	63.734	63.713	12.633	12.612
$\widehat{\mathbf{J}}_{12}^{rr}$ Tangential	-2.557	-2.556	-0.545	-0.544
$\widehat{\mathbf{J}}_{12}^{rr}$ Normal	2.936	2.936	0.934	0.934
$\widehat{\mathbf{J}}_{11}^{tr}$	4.957	4.953	0.713	0.710
$\widehat{\mathbf{J}}_{12}^{tr}$	7.755	7.760	2.330	2.333

We refer to the eigen value $\widehat{J}_{ij}^{tt\perp}$ or $\widehat{J}_{ij}^{rr\perp}$ along the line of separation as normal component. In contrast, the degenerated $\widehat{J}_{ij}^{tt\parallel}$ or $\widehat{J}_{ij}^{rr\parallel}$ in the plane tangential to the spheres at the point of minimum separation is denoted as tangential component.

The symmetry of the system also dictates that there are only one independent non-zero elements in each of the translation-rotation coupling tensors. These antisymmetric tensors are defined in two groups: 1) $\widehat{\mathbf{J}}_{11}^{tr} = \widehat{\mathbf{J}}_{22}^{tr} = \widehat{\mathbf{J}}_{11}^{rt\dagger} = -\widehat{\mathbf{J}}_{22}^{rt\dagger}$, and 2) $\widehat{\mathbf{J}}_{12}^{tr} = -\widehat{\mathbf{J}}_{21}^{tr} = \widehat{\mathbf{J}}_{21}^{rt\dagger} = -\widehat{\mathbf{J}}_{12}^{rt\dagger}$, where both can be uniquely described by the following form

$$\widehat{\mathbf{J}}_{ij}^{tr} = \widehat{J}_{ij}^{tr} \mathbf{E} \cdot \hat{\mathbf{e}}_z. \quad (29)$$

Here \widehat{J}_{ij}^{tr} represents the antisymmetric translation-rotation coupling with \mathbf{E} being the third order permutation tensor.

Simulated values of all non-trivial components of the mentioned tensors are displayed in Table 1. We use $\Omega = 10^{-5}$ in the algorithm outlined in the current article to get one set of values. The second set of results are obtained by using well documented Stokesian analysis [30]. The maximum relative departure between two sets are below 1%.

We check the two sets of simulations for two closely situated spheres ($s = 2.1$) as well as

the moderately separated ones ($s = 3$). The former is a more difficult convergence compared to the latter. To attain the same level of accuracy, we chose maximum spectral order l_{max} to be 32 and 16 in the frequency-dependent simulation for the respective cases. The frequency-independent Stokesian computation is especially well-converged for both cases, because it complements the basis function expansion with lubrication theory. Even though the corresponding lubrication analysis is not yet available for the unsteady dynamics, the level of accuracy captured solely by basis function expansion is indeed impressive indicating the reliability of the new methodology.

The designed validation under zero frequency limit ensures the correct starting values for subsequent plots describing spectral variations of friction. Such dependence on frequency ultimately quantifies how much unsteady systems depart from Stokesian dynamics.

B. Translational friction tensors

The new methodology is used to explore the frequency-dependent friction coefficients for a wide range of frequency Ω as well as separation distance s . We plot the independent eigen values of translation-translation tensors in Figs.1 and 2 as a function of Ω for four different values of s .

In Fig.1, the real values of tangential and normal eigen-values of both self and mutual translation-translation tensors are plotted. In contrast to Stokesian analysis, frequency-dependent friction tensors are complex numbers indicating an inertia-induced phase lag between force and motion. The corresponding imaginary parts of respective friction coefficients are presented in Fig.2.

We try to find s -dependent renormalization factors for the frictions as well as for the dimension-less Ω to make renormalized curves for different s collapse into a narrow band. The dependence of such factors with separation s is displayed in each subfigure. These expressions reveal the underlying physics involving the nature of the flow dynamics.

We notice that real values of friction for tangential self translation do not require any renormalization exhibiting minimal effect of the neighboring sphere. It is to be noted that for quasi-steady Stokesian dynamics these coefficients have a very weak logarithmic increase with decreasing surface-to-surface separation. Thus, for such quantities, the flow induced in inertial boundary layer outside the lubrication region is mainly responsible for creating

the resistance. Also, one can notice that the self-friction is consistently negative, as the viscous effect has to be purely resistive. It increases with frequency due to the creation of hindering fields caused by the fluid inertia in boundary layer manifesting Basset history force. This effect increases proportional to $\sqrt{\Omega}$ for high excitation frequencies because then Basset contribution scales as $\mu a^2/l_{md}$ with $l_{md} = a/\sqrt{\Omega}$ being the length-scale for momentum diffusion. The lack of variations with s as well as curvatures in the plots make the expected proportionality with $\sqrt{\Omega}$ evident in Fig.1.

The spectral dependence of normal self friction is similar to the corresponding tangential component except in the low frequency Stokesian limit. For very slow oscillations, the main contribution in hydrodynamic resistance appears due to viscous effects in the lubrication region at the narrowest gap between the two spheres. Such Stokesian friction in non-dimensional form scales as $a/(s - 2a) = 1/(\tilde{s})$ [31]. Thus, we rescale normal eigen value of \mathbf{J}_{11}^{tt} by multiplying with \tilde{s} . For high frequency regime, however, the inertial Basset scaling dictates a proportionality to $\sqrt{\Omega}$. We can restore this expected behavior by re-normalizing Ω by its product with \tilde{s}^2 . As a result, one can see that the curves for normal self friction collapsed properly in Fig.1 irrespective of separation values.

Unlike self frictions, the mutual tangential friction is positive for low frequencies showing how one body can be dragged by the other in the direction of its motion in accordance to the Stokesian dynamics. The mutual coefficients, however, become negative for larger frequency, when inertia-induced recirculating fields become stronger for quicker fluctuations. Such effect remains proportional to $\sqrt{\Omega/\tilde{s}}$ with the factor $\sqrt{1/\tilde{s}}$ being multiplied to Basset scaling $\sqrt{\Omega}$ to account for impact of particulate separations on mutual interactions. We notice that the interplay between the direct viscous stress and the opposing inertial field flip the curves to negative value at a cross-over frequency scaled with \tilde{s} . One should note that the non-dimensional Ω is obtained by multiplying the nominal time-scale $a^2\rho/\mu$ with excitation frequency, where the natural length-scale is assumed as a . The introduction of the renormalization of Ω by multiplying with \tilde{s} reveals a new time-scale in the form of $a(s - 2a)\rho/\mu$ indicating a new length-scale $\sqrt{a(s - 2a)}$ for the problem. We immediately recognize this new dimension as the radial extent of the lubrication domain in between two bodies manifesting the enhanced importance of the near-contact region. This implies that the interplay between the lubrication dynamics and the inertia-induced fields outside the contact region dictates the behavior of the mutual influence in tangential direction. When

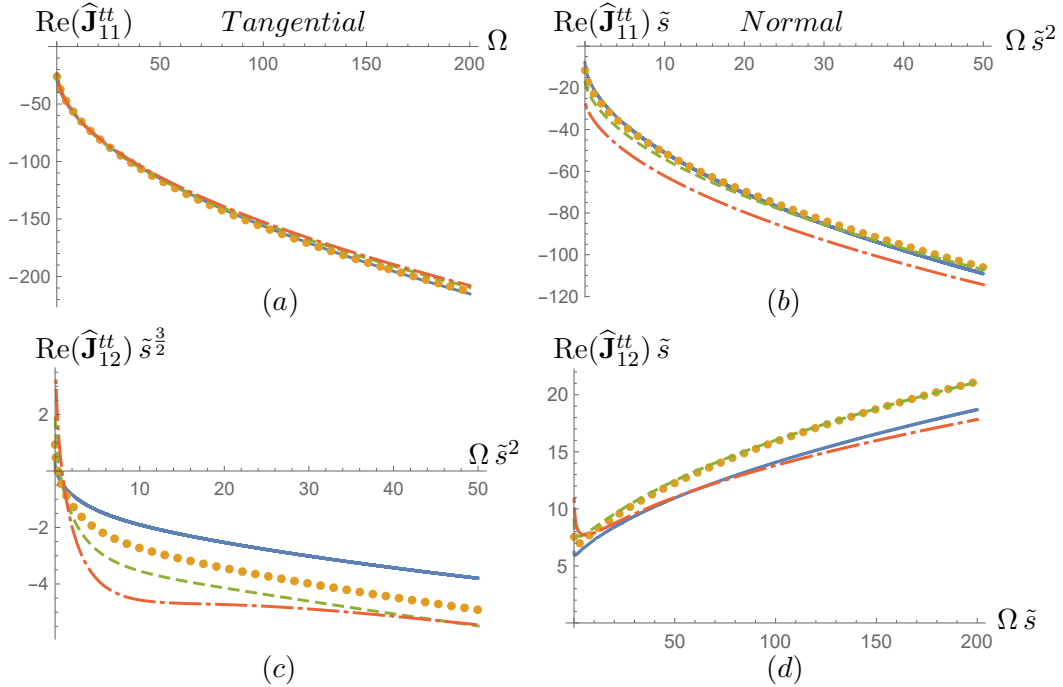


FIG. 1. Normalized non-zero real part of translational friction $\widehat{\mathbf{J}}_{11}^{tt}$ or $\widehat{\mathbf{J}}_{12}^{tt}$ is plotted as a function of natural frequency Ω under tangential (left panel) or normal (right panel) incitement with center-to-center separation $s = 2.1$ (solid line), $s = 2.25$ (solid dotted line), $s = 2.5$ (dashed line) and $s = 3$ (dot-dashed line). Surface-to-surface separation \tilde{s} is renormalized factor defined as $\tilde{s} = s - 2$.

the aforementioned re-normalization of the abscissa is coupled a multiplicative factor of $\tilde{s}^{3/2}$ to the ordinate, proportionality to $\sqrt{\Omega/\tilde{s}}$ for large Ω can be captured. This fact is attested by Fig.1, where the curves are group together closely except the purely Stokesian values at $\Omega=0$.

The normal translational mutual frictions does not show any cross-over – it is always positive indicating the thrust created by the moving body on the static one. In absence of any cross-over, we use lubrication scaling $1/\tilde{s}$ for normal motion to rescale the frictional coefficient by multiplying it by \tilde{s} . Then, the high-frequency Basset contribution requires the abscissa to be multiplied by \tilde{s} so that proportionality to $\sqrt{\Omega/\tilde{s}}$ is properly represented. Such replotting immediately produced closely clustered curves.

The competitive interplay between inertia and viscous lubrication is subdued in Fig.2, as the imaginary part of the friction only appears due to the former for an unsteady system. This is why all the curves approach 0 when $\Omega \rightarrow 0$ in Fig.2. For finite Ω , the imaginary part of the self-friction is most affected by the fluid acceleration especially in the boundary layer around the entire sphere. This effect akin to "added mass term" is proportional to

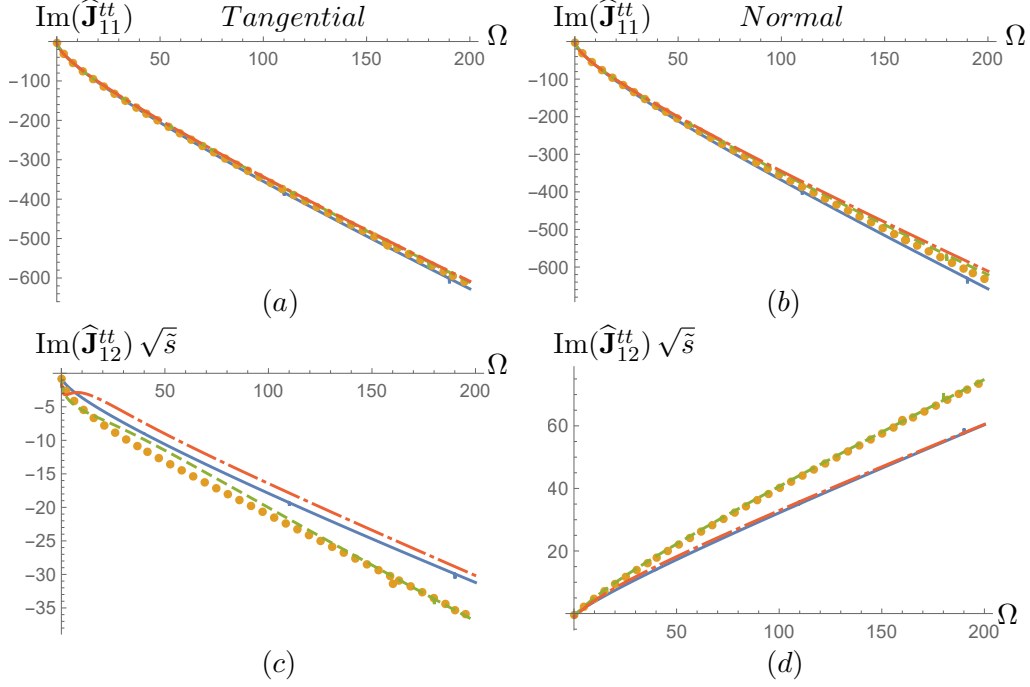


FIG. 2. Normalized non-zero imaginary part of translational friction $\widehat{\mathbf{J}}_{11}^{tt}$ or $\widehat{\mathbf{J}}_{12}^{tt}$ is plotted as a function of natural frequency Ω under tangential (left panel) or normal (right panel) incitement with center-to-center separation $s = 2.1$ (solid line), $s = 2.25$ (solid dotted line), $s = 2.5$ (dashed line) and $s = 3$ (dot-dashed line). Surface-to-surface separation \tilde{s} is renormalized factor defined as $\tilde{s} = s - 2$.

Ω irrespective of s explaining closely grouped straight line plots for self elements in Fig.2. The boundary-layer around the entire sphere is not, however, important, when the sphere is not moving. Then, the part of this layer inside the contact region predominantly affects force on the static body. Thus, the imaginary part of mutual friction grows relatively more with the increasing proximity to the moving sphere. Such increase is represented by the product of the non-dimensional friction and $\sqrt{\tilde{s}}$ in Fig.2. The positivity and negativity of the quantities in Fig.2 is consistent with Fig.1 implying proper satisfaction of causality.

C. Rotational friction tensors

We present independent eigen values of rotational frictions in Figs.3 and 4. In Fig.3, their real parts are plotted, whereas Fig.4 displays the imaginary parts. All plots are renormalized with appropriate s -dependent factors to ensure the coherent collapse of the curves.

As seen for the tangential self translational tensor in Fig.2, real parts of both eigen

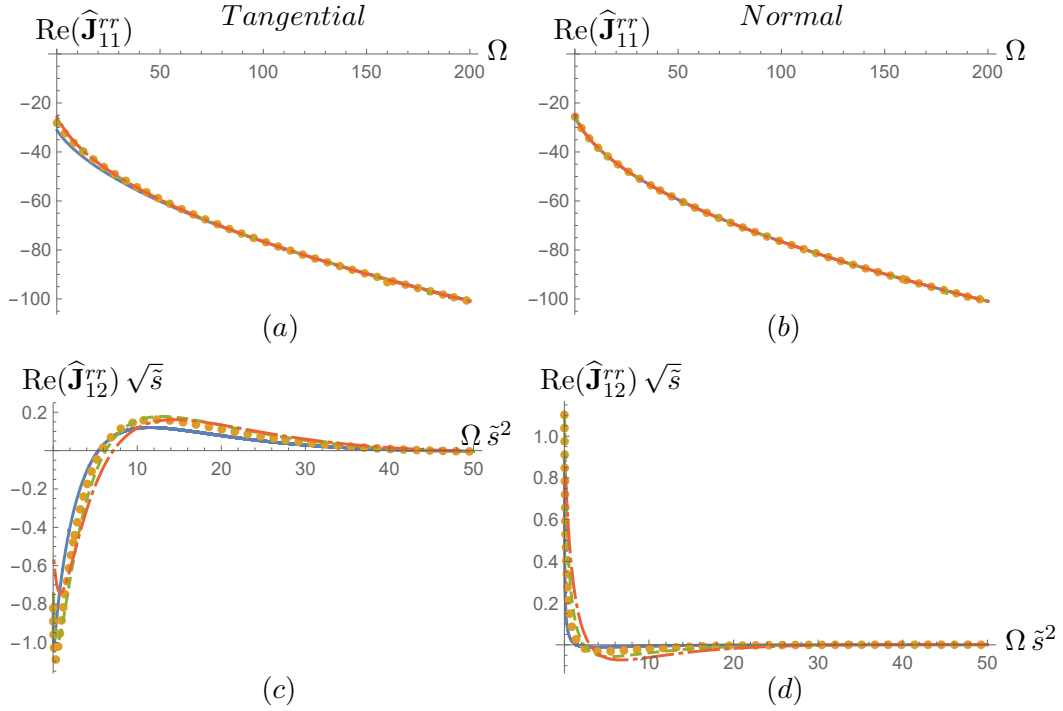


FIG. 3. Normalized non-zero real part of rotational friction $\hat{\mathbf{J}}_{11}^{rr}$ or $\hat{\mathbf{J}}_{12}^{rr}$ is plotted as a function of natural frequency Ω under tangential (left panel) or normal (right panel) incitement with center-to-center separation $s = 2.1$ (solid line), $s = 2.25$ (solid dotted line), $s = 2.5$ (dashed line) and $s = 3$ (dot-dashed line). Surface-to-surface separation \tilde{s} is renormalized factor defined as $\tilde{s} = s - 2$.

values of rotational counterparts do not need any renormalization of either the abscissa or the ordinate. This means that viscous stresses in lubrication region has a weaker impact on self rotational resistance. On contrary, the main contribution in $\hat{\mathbf{J}}_{11}^{rr}$ comes from the Basset history caused by inertial boundary-layer over the entire sphere. As a result, the simulated results for $\hat{\mathbf{J}}_{11}^{rr}$ exhibit negligible variation with s as well as proportionality to $\sqrt{\Omega}$ for large frequency. Also, their negative values manifest resistive nature of the surrounding fluid.

The mutual rotational frictions, however, require renormalizations of both the abscissa and the ordinate. The rescaling factor for Ω is \tilde{s}^2 indicating a new time-scale $(s-2a)^2\rho/\mu$ or a characteristic length as surface-to-surface separation $(s-2a)$. This implies the importance of the direct viscous interactions in the lubrication region to be the primary mechanism responsible for transmission of torque from the rotating sphere to the static one. As a result, both components of mutual rotational friction recover renormalization factor which should be a logarithmic function of \tilde{s} according to lubrication theory. We find such factor a little problematic to handle as it goes to 0 for $s=3a$. Thus, we choose a function weaker than $1/\tilde{s}$ to multiply with the ordinate leading to a reasonable clustering of the curves.

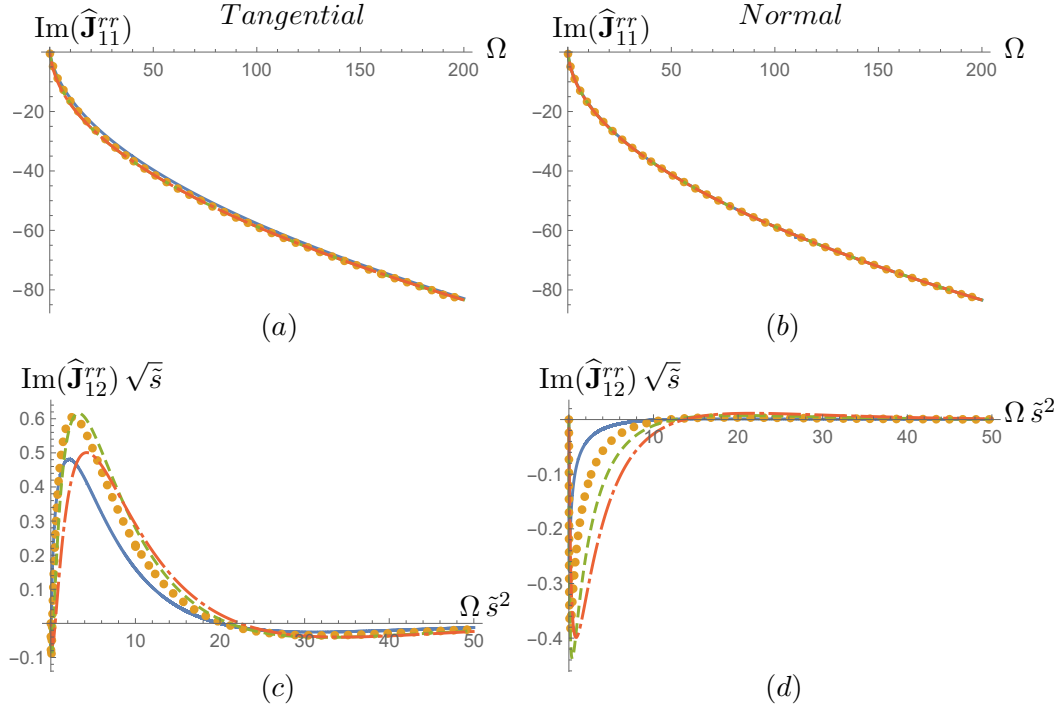


FIG. 4. Normalized non-zero imaginary part of rotational friction $\widehat{\mathbf{J}}_{11}^{rr}$ or $\widehat{\mathbf{J}}_{12}^{rr}$ is plotted as a function of natural frequency Ω under tangential (left panel) or normal (right panel) incitement with center-to-center separation $s = 2.1$ (solid line), $s = 2.25$ (solid dotted line), $s = 2.5$ (dashed line) and $s = 3$ (dot-dashed line). Surface-to-surface separation \tilde{s} is renormalized factor defined as $\tilde{s} = s - 2$.

Both mutual components display an interplay between viscous interactions in lubrication region and Basset contribution from the inertial boundary layer in the same location. The former being stronger in Stokes regime tries to drive the fixed sphere following the motion of the driver at the near-contact point. The latter, however, grows larger for higher frequencies, and creates an opposing effect due to inertia generated fields. Such counter-balancing dynamics is evident in Fig.3, where all curves for mutual rotational friction change sign.

For rotational motions, the phase lag between the torque and the angular velocity is mainly caused by Basset term, as added mass is irrelevant for axisymmetric revolution. Accordingly, one can see the similarity between the real and imaginary parts of the rotational frictions for high frequency values as described by Figs.3 and 4, respectively. For low frequencies, the imaginary parts vanish predictively as evident in Fig.4. It is obvious from Fig.4 that the imaginary parts of the self rotation friction is caused by the entire inertial layer across the spherical surface. On the contrary, the same for the mutual one is most influenced by the acceleration induced fields at the contact region.

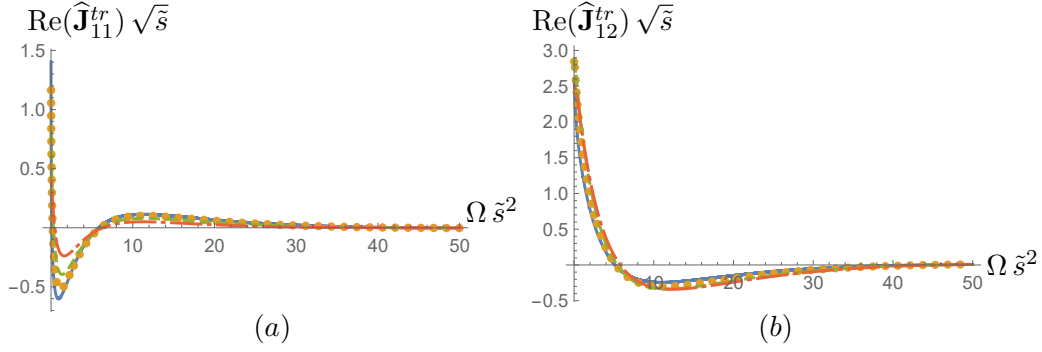


FIG. 5. Normalized non-zero real part of translation-rotation friction $\hat{\mathbf{J}}_{11}^{tr}$ or $\hat{\mathbf{J}}_{12}^{tr}$ is plotted as a function of natural frequency Ω with center-to-center separation $s = 2.1$ (solid line), $s = 2.25$ (solid dotted line), $s = 2.5$ (dashed line) and $s = 3$ (dot-dashed line). Surface-to-surface separation \tilde{s} is renormalized factor defined as $\tilde{s} = s - 2$.

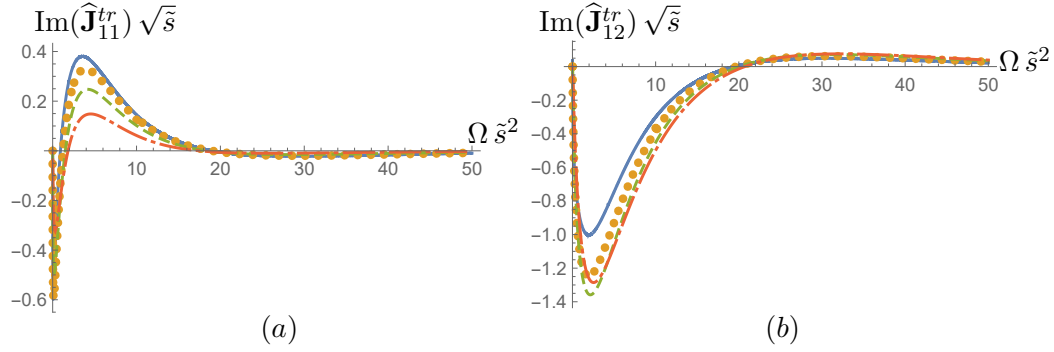


FIG. 6. Normalized non-zero imaginary part of translation-rotation friction $\hat{\mathbf{J}}_{11}^{tr}$ or $\hat{\mathbf{J}}_{12}^{tr}$ is plotted as a function of natural frequency Ω with center-to-center separation $s = 2.1$ (solid line), $s = 2.25$ (solid dotted line), $s = 2.5$ (dashed line) and $s = 3$ (dot-dashed line). Surface-to-surface separation \tilde{s} is renormalized factor defined as $\tilde{s} = s - 2$.

D. Translation-rotation couplings

In Figs.5 and 6, the real and the imaginary parts of the only independent component in antisymmetric translation-rotation coupling tensors are presented. Both the self and the mutual frictions are plotted as functions of frequency for different separations in either these figures. Like translational and rotational frictions, the renormalization factors for proper collapse of the curves are indicated in the plots.

In both Figs.5 and 6, the renormalization of the frequency implies that the translation-rotation coupling occurs due to direct viscous as well as inertial interactions in near-contact region. This is an expected conclusion as rotation can generate force only in presence of a

neighboring particle in close proximity. As a result, the curves in Figs.5 and 6 has qualitative similarities with mutual rotational frictions in Figs.3 and 4, respectively.

IV. TIME-DEPENDENT MOBILITY RESPONSE

The frequency-dependent frictions presented in section III imply a delayed action of motion-instigating quantities like force and torque on the particulate dynamics. This means that if any solid body encounters an impulse in an inertial viscous fluid, its motion depends not only on the instantaneous force or torque but also their history. Such retarded response can be expressed by following convolutions:

$$\mathbf{u}_i(t) = \int_0^t \left\{ \sum_j [\mathbf{K}_{ij}^{tt}(t_0) \cdot \mathbf{f}_j^e(t-t_0) + \mathbf{K}_{ij}^{tr}(t_0) \cdot \boldsymbol{\tau}_j^e(t-t_0)] \right\} dt_0, \quad (30)$$

and

$$\boldsymbol{\omega}_i(t) = \int_0^t \left\{ \sum_j [\mathbf{K}_{ij}^{rt}(t_0) \cdot \mathbf{f}_j^e(t-t_0) + \mathbf{K}_{ij}^{rr}(t_0) \cdot \boldsymbol{\tau}_j^e(t-t_0)] \right\} dt_0. \quad (31)$$

Here, \mathbf{f}_j^e and $\boldsymbol{\tau}_j^e$ represent given external force and torque exerted on the j -th particle, whereas $\mathbf{K}_{ij}^{pq}(t)$ is time-dependent mobility tensors.

In this section, we compute unsteady mobility tensors \mathbf{K}_{ij}^{pq} as temporal functions describing motions due to a force or a torque proportional to dirac delta function in time. The simulations consider four different initial separations between two particles of interest. As a result, one can estimate how a Brownian sphere moves in presence others, when instigated by an impulsive force or torque in presence of fluid inertia. It also shows how it creates flow fields around its vicinity to affect neighboring suspended solid over time.

A. Construction of Physical Mobility Matrix

The Fourier transforms of eqs.30 and 31 yield the following relations:

$$\hat{\mathbf{u}}_i(\Omega) = \sum_j [\hat{\mathbf{K}}_{ij}^{tt}(\Omega) \cdot \hat{\mathbf{f}}_j^e(\Omega) + \hat{\mathbf{K}}_{ij}^{tr}(\Omega) \cdot \hat{\boldsymbol{\tau}}_j^e(\Omega)] \quad (32)$$

and

$$\hat{\boldsymbol{\omega}}_i(\Omega) = \sum_j [\hat{\mathbf{K}}_{ij}^{rt}(\Omega) \cdot \hat{\mathbf{f}}_j^e(\Omega) + \hat{\mathbf{K}}_{ij}^{rr}(\Omega) \cdot \hat{\boldsymbol{\tau}}_j^e(\Omega)]. \quad (33)$$

Here, $\hat{\mathbf{K}}_{ij}^{pq}$ is the frequency-dependent amplitude obtained from time-dependent \mathbf{K}_{ij}^{pq} in Fourier space, whereas $\hat{\mathbf{f}}_j^e$ and $\hat{\boldsymbol{\tau}}_j^e$ are the same for \mathbf{f}_j^e and $\boldsymbol{\tau}_j^e$. The equalities in eqs.32 and 33 are derived using the property stating that transformed convolution is product of transformations.

The force or torque balance equations for each sphere relate motion-inducing and motion-defining quantities in an alternative way. Accordingly,

$$m_i \frac{d\mathbf{u}_i(t)}{dt} = \mathbf{f}_i(t) + \mathbf{f}_i^e(t), \quad L_i \frac{d\boldsymbol{\omega}_i(t)}{dt} = \boldsymbol{\tau}_i(t) + \boldsymbol{\tau}_i^e(t), \quad (34)$$

where m_i and L_i stand for mass and moment of inertia of the i -th spherical particle, respectively. Also, \mathbf{f}_j and $\boldsymbol{\tau}_j$ are viscous force and torque already defined in eq.23.

As a result, the Fourier transform of eq.34 along with eq.26 ensures:

$$\sum_j [\{i\Omega m_i - \hat{\mathbf{J}}_{ij}^{tt}(\Omega)\} \cdot \hat{\mathbf{u}}_j(\Omega) - \hat{\mathbf{J}}_{ij}^{tr}(\Omega) \cdot \hat{\boldsymbol{\omega}}_j(\Omega)] = \hat{\mathbf{f}}_i^e(\Omega) \quad (35)$$

$$\sum_j [-\hat{\mathbf{J}}_{ij}^{rt}(\Omega) \cdot \hat{\mathbf{u}}_j(\Omega) + \{i\Omega L_i - \hat{\mathbf{J}}_{ij}^{rr}(\Omega)\} \cdot \hat{\boldsymbol{\omega}}_j(\Omega)] = \hat{\boldsymbol{\tau}}_i^e(\Omega). \quad (36)$$

We recognize that eqs.32 and 33 are exactly equivalent to eqs.35 and 36. The former set of linear relations can be obtained by simply inverting the latter set. Accordingly, we invert the linear relations in eqs.35 and 36 to find the frequency-dependent mobility tensors $\hat{\mathbf{K}}_{ij}^{pq}$. Finally, the inverse Fourier transform of $\hat{\mathbf{K}}_{ij}^{pq}$ render the time-dependent mobility response tensor

$$\mathbf{K}_{ij}^{pq}(t) = \frac{1}{2\pi} \int_{-\infty}^{\infty} \hat{\mathbf{K}}_{ij}^{pq}(\Omega) \exp(i\Omega t) d\Omega, \quad (37)$$

which also represent the motions instigated by impulsive force or torque.

The non-dimensional mass m_i and momentum inertia L_i for spheres are $(4\pi/3)\bar{\rho}$ and $(8\pi/15)\bar{\rho}$ with $\bar{\rho}$ being the ratio of densities of the suspended solids and the surrounding fluids. In our simulation, we consider neutrally buoyant particles with exact same density of the liquid inferring $\bar{\rho}=1$. We construct the linear relations in eqs.35 and 36 accordingly, and invert it to compute $\hat{\mathbf{K}}_{ij}^{pq}$. Then, eq.37 is used to find the non-zero normal and tangential eigen components of the mobility response tensors as functions of time.

The presented plots provide answers to outstanding questions in particulate hydrodynamics by showing when and by what extent unsteady inertial effects are significant in many-body dynamics. We choose the temporal range along the abscissa based on the duration in which transiency is important. Such period is dictated by the saturation of the curves to zero. This implies the validity of Stokesian dynamics after the time displayed in the subsequent figures. It is to be noted though that a purely non-inertial Stokesian dynamics cannot handle impulses. Thus, the connection between the presented results under the action of impulses and non-inertial viscous systems should be interpreted in integral sense.

In other words, area under the curves produced here by delta function force or torque is same as the Stokesian mobility under constant instigations. Consequently, when our time-dependent curves saturate to zero beyond the displayed range, unsteady contributions do not create any major impact on the motion.

B. Translational response tensors revealing delayed action

The eigen values of translation-translation mobility response tensor in tangential and normal directions are plotted in Fig.7 as functions of time. These represent the rectilinear velocity for both spheres induced by a force impulse on one of them. The transient rate of translation of the particle interacted with the impulse is referred as self mobility, whereas the same for the other is called mutual response. Thus, the components for both the self and mutual tensors are presented in Fig.7 for four different separation distance between the two particles.

As expected, the self response is a consistently decaying temporal function suggesting that the impact of a past impulse would gradually wane. The effect of the other sphere on self mobility is not pronounced, though a closer proximity to it exhibits less velocity. This decrease is understandable as the second sphere always tries to constrict the motion of the first. The normal component is more affected by the other body due to a head-on interactions causing stronger lubrication resistance.

For mutual response, the temporal variation is not monotonic. The associated curves always start from 0 at the initial time when the impact of the impulse have not been transmitted via the fluid medium to the neighboring particle. The starting value is not apparent in Fig.7 simply because the quantity reaches to non-zero values in a very short time. The normal component first increases, when the flow induced in the fluid takes time to reach the other particle. Then, it started to decrease in a similar manner seen for the self components. As the normal component is created by a head-on interactions, it remains positive always implying the neighboring sphere is directly driven by the instigated particle. In contrast, the tangential component of the mutual tensor is initially negative meaning that at the start, the recirculating fluid ensuring volumetric conservation drives the neighbor backward. However, soon the fluid starts to circumvent the solid bodies at a greater distance causing a similar motion between the driver and the driven. At this time, mutual tangential

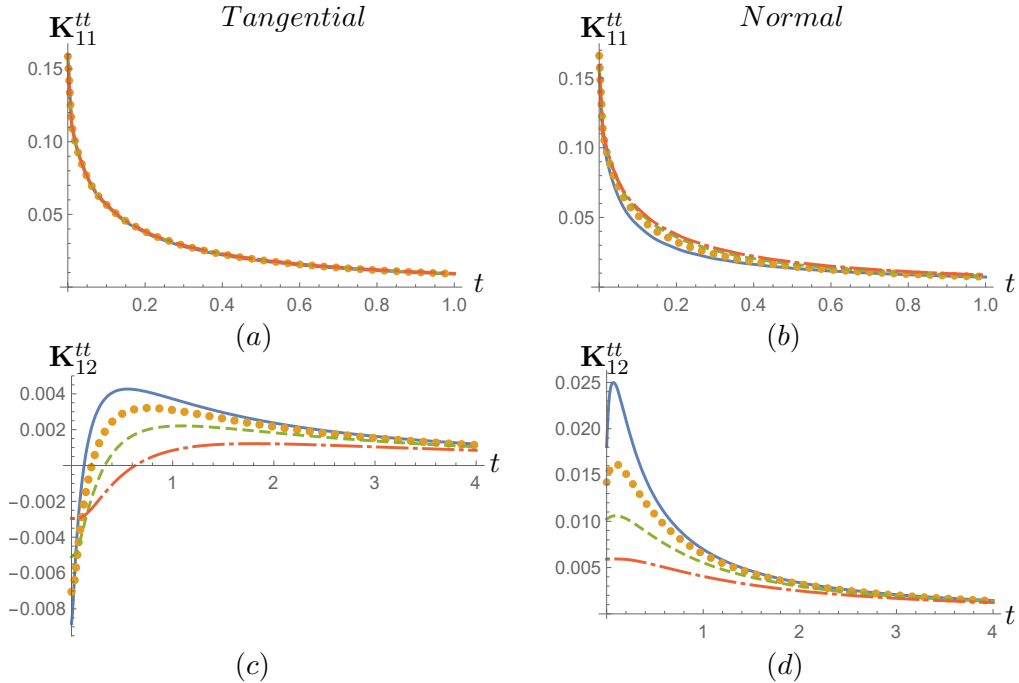


FIG. 7. Normalized non-zero translational mobility \mathbf{K}_{11}^{tt} or \mathbf{K}_{12}^{tt} is plotted as a function of time under tangential (left panel) or normal (right panel) incitement with center-to-center separation $s = 2.1$ (solid line), $s = 2.25$ (solid dotted line), $s = 2.5$ (dashed line) and $s = 3$ (dot-dashed line).

components flip sign to become positive. For both components, a more closely situated configurations create more pronounced impact on the driven.

When time tends to 0, the self friction approaches to a value $1/(2\pi)$. This can be predicted from the instantaneous effect of force-impulse on immediate ballistic motion. For translation of neutrally buoyant sphere, its mass $4\pi/3$ is complemented by an added mass $2\pi/3$ from fluid causing the net inertia to be 2π . A unit impulse, then should produce a velocity of $1/(2\pi)$ which is replicated by the simulation. Such corroboration proves the accuracy of the presented algorithm in the short-time range, whereas the validations in subsection 3.1 correspond to large temporal scales. Thus, the two complimentary sets of quantitative verification in two different regimes vouch for the correctness and versatility of the methodology.

C. Transient rotational response

In Fig.8, the eigen components of rotation-rotation mobility response in tangential and normal directions are plotted as functions of time. This shows how angular velocity is induced for both particles when one of them encounters an impulsive unit torque. Accord-

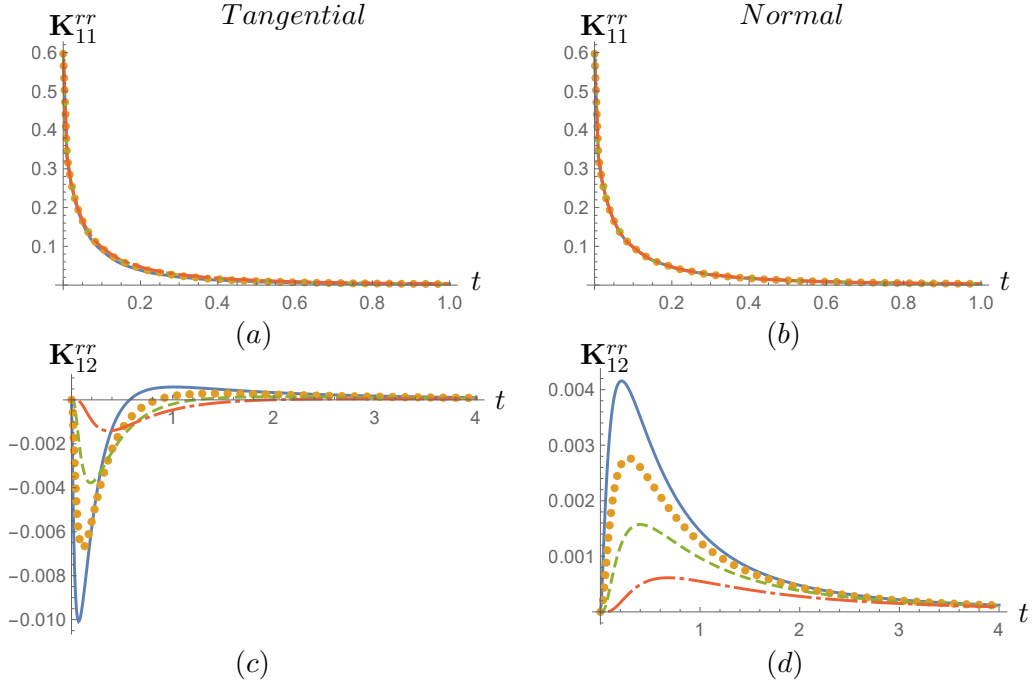


FIG. 8. Normalized non-zero rotational mobility \mathbf{K}_{11}^{rr} or \mathbf{K}_{12}^{rr} is plotted as a function of time under tangential (left panel) or normal (right panel) incitement with center-to-center separation $s = 2.1$ (solid line), $s = 2.25$ (solid dotted line), $s = 2.5$ (dashed line) and $s = 3$ (dot-dashed line).

ingly, Fig.8 describes both the self and mutual mobility tensors. Like in Fig.7, the results are presented for four different separation distances.

If Figs.7 and 8 are compared, the corresponding plots are qualitatively very similar. The self rotational mobility response decays monotonically with time, and shows negligible relative variations for inter-particle separation distance. In contrast, the mutual rotational tensor components show first increasing and then decreasing temporal variations with 0 being the starting value. One significant difference between translational and rotational mutual response is a longer time needed by the latter for reaching a maximum value signifying a slower development of recirculating flow.

For time tending to 0, the simulated results show the self rotational mobility to be 0.5972. This value approximately matches with $15/(8\pi)$ which is the inverse of non-dimensional moment of inertia L_i for neutrally buoyant particles. It is to be noted that for rotational motion there is no additional inertia due to fluid as seen for translation in the form of added mass. Thus, it is expected that the angular velocity created by an impulse of unit torque to be $1/L_i$ which is corroborated by the simulation. As discussed for translational dynamics, this validation for rotational mobility under short-time limit provides additional confidence in versatility and accuracy of the presented algorithm.

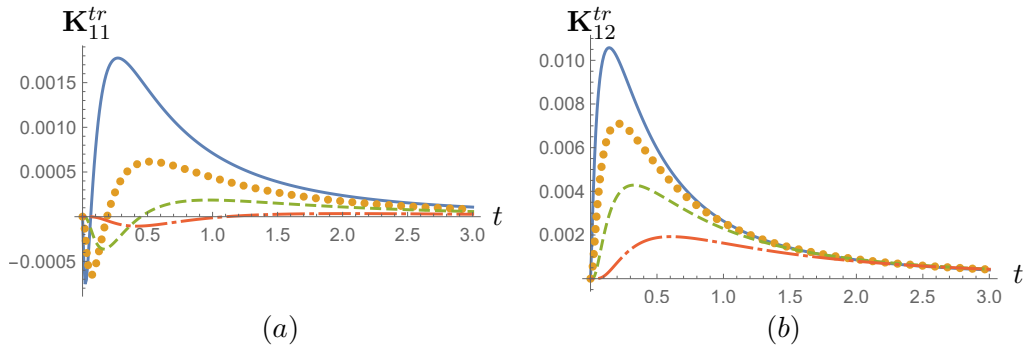


FIG. 9. Normalized non-zero translation-rotation mobility \mathbf{K}_{11}^{tr} or \mathbf{K}_{12}^{tr} is plotted as a function of time with center-to-center separation $s = 2.1$ (solid line), $s = 2.25$ (solid dotted line), $s = 2.5$ (dashed line) and $s = 3$ (dot-dashed line).

D. Unsteady translation-rotation mobility coupling

For two-body systems in fluid, an impulsive tangential force on one particle can produce delayed rotation of both. Conversely, an impulsive tangential torque can cause rectilinear motion. Such phenomena are described in Fig.9 by translation-rotation coupling response \mathbf{K}_{pq}^{tr} or \mathbf{K}_{pq}^{rt} .

Due to geometric symmetry, \mathbf{K}_{pq}^{tr} or \mathbf{K}_{pq}^{rt} are antisymmetric matrices like the friction counterparts \mathbf{J}_{pq}^{tr} or \mathbf{J}_{pq}^{rt} with axis of symmetry being the direction of eigen value 0. Moreover, reciprocal theorem ensures that \mathbf{K}_{pq}^{tr} is transpose of \mathbf{K}_{qp}^{rt} . Our simulation results independently verifies these relations. Thus, the translation-rotation coupling can be uniquely described by one self function K_{11}^{tr} and one mutual one K_{12}^{tr} . These two quantities are plotted in Fig.9 for four different separation distances.

Translation-rotation coupling appears purely due to the mutual interactions, as this effect disappears for isolated single sphere in free-space. Consequently, both plots in Fig.9 exhibit qualitative similarity with the mutual mobility responses seen in Figs.7 and 8. Initially, all curves in Fig.9 start from 0 because the presence of the second particle would not be felt until the fluid transmits the field. Then, the self coefficient would initially becomes negative as majority of the recirculation has to occur through the region not constricted by the neighboring solid body. In the later time, however, the recirculation zone expands beyond the particulate dimension, so that the pair can rotate as a group causing a reversal in K_{11}^{tr} . In contrast, K_{12}^{tr} is always positive manifesting how the driven body rotates in sync with the translation of the driver.

V. SUMMARY AND CONCLUDING REMARKS

This article presents a methodology to analyze time-dependent hydrodynamic interactions among many solid spheres in a viscous fluid. The formulation accounts for both transient inertia as well as viscous stresses, while ignores nonlinear convective acceleration assuming low Reynolds number. The consequent linearized but unsteady Navier-Stokes equation is solved to compute the fields inside the infinite fluid domain in presence of solid spheres. The ultimate goal of the analysis is to find the motions of all particles as temporal functions when one of these are instigated by a time-dependent force or torque.

The aforementioned analysis is completed in a four-step mathematical procedure. Firstly, the hydrodynamic fields are expanded in separable forms with temporal Fourier functions and time-invariant but spatially varying eigen solutions for Brinkman equation. Then, transformations between two sets of such spatially dependent eigen functions centered at two different spheres are derived. Thirdly, the provided boundary conditions are exploited to form a set of algebraic relations from which the frequency-dependent friction tensors are constructed. Finally, the computed frictions are inserted into equation of motion for translation and rotation of each sphere to describe their transient motion in terms of mobility response tensors.

The discussed algorithm is used to compute delayed motion of two spheres when one of these has encountered an impulsive force or torque in an earlier time. Both particles are assumed to satisfy no-slip boundary conditions at their solid-liquid interfaces. These are considered to be neutrally buoyant with exact same density as the surrounding liquid. Our simulation results include the frequency-dependent self and mutual frictions which give the force or torque on a moving sphere as well as on a fixed neighbor respectively. Also, the unsteady self and mutual mobilities are computed to show how an impulse can directly make a particle move or indirectly induce motion of a neighbor via the medium.

We validate our computation by using two different known results for two mutually exclusive regimes. Firstly, the friction coefficients under the limit of low frequency is verified by benchmark Stokesian dynamics findings. Secondly, the initial motion induced immediately after the action of a force or torque impulse is checked by considering particle inertia and added mass due to the fluid flow. Both tests show our simulation to be accurate with relative error around 0.1%. The first validation corresponds to long-time behavior, whereas

the second one vouches for the accuracy in description of the short-time dynamics. Thus, such mutually independent verifications exhibit the robustness and versatility of the outlined algorithm.

The frequency-dependent frictions presented in this paper reveal the underlying physics of the flow-dynamics. To capture this, we plot frictions as functions of frequency for different interparticle distance. Then, both abscissa and ordinate are renormalized by factors dependent on the separation width so that the curves collapse into narrow bands. The renormalization factors for both x and y axes indicate what effect is the predominant contributors in what frequency. As expected, we see low-frequency values of real parts in the self resistances are mainly impacted by viscous stresses especially at the narrowest gap between two bodies. The corresponding high-frequency behaviors are, however, dictated by Basset history force due to fluid inertia around the particles. We have also seen that spectral variations in the imaginary parts of these quantities can be explained by extra inertia caused by added mass of the liquid domain. Such inertial effects are typically manifested by negligible dependence on separation distance and monotonic power-law variation with frequency. Interestingly, more complicated interplay between viscous and inertial effects can be observed in the coefficients which appear only due to the presence of a neighboring second particle. Accordingly, one can see non-monotonic curves for mutual tensors as well as in translation-rotation coupling parameters. The opposing contributions from direct lubrication and inertia-induced recirculating fields often create reversal in these quantities as evident in their plots.

The spectral variations in frictions has corresponding ramifications in temporal dependence of mobility responses. This is why one can see gradual and consistent decrease in translational and rotational self mobilities indicating the waning impact of an initial impulse. The other coefficients only appearing due to the second sphere show an initial increases indicating delayed transmission through the fluid medium. Then, a subsequent decay manifests the dissipation of the initial agitation. The previously mentioned interplay between the direct lubrication stresses and inertia-induced recirculation also causes reversal in sign for some of these quantities.

The developed algorithm to analyze many-body unsteady hydrodynamic interactions would be a crucial tool in a number of contemporary fluid mechanical studies. This can be immediately used to quantitatively predict nano-fluidic properties by accounting for the

cumulative microscopic flow fluctuations induced by many Brownian bodies. Also, one can apply our methodology to estimate the correction needed in micro-rheological theory, if multiple tracer particles affect each other. Similarly, filtration simulations in inhomogeneous porous medium with large obstacles and porous matrix can import the presented formulation. We are planning to explore and expand such wide range of fields in the near future with the mathematical procedure narrated in this article.

ACKNOWLEDGMENTS

Acknowledgment: This work is supported by NSF grant CBET-1805930.

Data availability statement

The data that support the findings of this study are available from the corresponding author upon reasonable request.

Appendix A: Vectors to convert from functional to physical space

This appendix describes vector $\mathbf{v}_{ls}^{(m)P}$, $\mathbf{w}_{\lambda\sigma}^{(m)Q-}$ and $\mathbf{w}_{\lambda'\sigma'}^{(m)Q+}$ in eq.27 for all possible indices. The three quantities require three different sets of derivations.

Firstly, we focus on the expression of velocity $\mathbf{v}_{ls}^{(m)P}$ which are simply identified from the specified boundary condition corresponding to the considered motion. For translation of a sphere, there only exists 6 non-zero elements in $\mathbf{v}_{ls}^{(m)t}$, which are given by:

$$\mathbf{v}_{12}^{(1)t} = \mathbf{v}_{13}^{(1)t} = -\frac{1}{2}\hat{\mathbf{e}}_x + \frac{i}{2}\hat{\mathbf{e}}_y, \quad \mathbf{v}_{12}^{(-1)t} = \mathbf{v}_{13}^{(-1)t} = \hat{\mathbf{e}}_x + i\hat{\mathbf{e}}_y, \quad \mathbf{v}_{12}^{(0)t} = \mathbf{v}_{13}^{(0)t} = \hat{\mathbf{e}}_z. \quad (\text{A1})$$

In contrast, only three non-trivial elements in $\mathbf{v}_{ls}^{(m)r}$ contribute to rotation:

$$\mathbf{v}_{11}^{(1)r} = -\hat{\mathbf{e}}_x - i\hat{\mathbf{e}}_y, \quad \mathbf{v}_{11}^{(-1)r} = \frac{1}{2}\hat{\mathbf{e}}_x - \frac{i}{2}\hat{\mathbf{e}}_y, \quad \mathbf{v}_{11}^{(0)r} = \hat{\mathbf{e}}_z. \quad (\text{A2})$$

The eqs.A1 and eq.A2 give us all possible boundary conditions related to the motion of rigid sphere.

Secondly, we derive $\mathbf{w}_{\lambda'\sigma'}^{(m)Q+}$ representing force or torque generated by regular basis function. Net force can be derived by surface integral of stress at the spherical interface. Then

we apply divergence theorem to simplify our calculation whose details are as below:

$$\mathbf{w}_{\lambda'\sigma'}^{(m)t+} = \int_{p.s.} \hat{n} \cdot \bar{\bar{\sigma}}_{\lambda'm\sigma'} dA = \int_{p.v.} \nabla \cdot \bar{\bar{\sigma}}_{\lambda'm\sigma'} dV = i\Omega \int_{p.v.} \mathbf{v}_{\lambda'm\sigma'}^+ dV \quad (\text{A3})$$

where $\bar{\bar{\sigma}}_{\lambda'm\sigma'}$ represents fluid stress tensor, \hat{n} means normal unit vector pointing outward on the particle surface. The area integral on the particle surface is denoted by $\int_{p.s.} \dots dA$, whereas $\int_{p.v.} \dots dV$ is volumn integral inside the solid volume. Like $\mathbf{v}_{\lambda's}^{(m)t}$, most of elements in $\mathbf{w}_{\lambda'\sigma'}^{(m)t+}$ representing force disappear — the only non-zero elements correspond to $\lambda' = 1$, $\sigma' = 2, 3$ so that non-trivial components are given by:

$$\begin{cases} \mathbf{w}_{12}^{(1)t+} = \frac{8}{3}\pi k^2 (k \cosh k - \sinh k) \hat{\mathbf{e}}_x + \frac{8}{3}i\pi k^2 (k \cosh k - \sinh k) \hat{\mathbf{e}}_y \\ \mathbf{w}_{12}^{(0)t+} = -\frac{8}{3}\pi k^2 (k \cosh k - \sinh k) \hat{\mathbf{e}}_z \\ \mathbf{w}_{12}^{(-1)t+} = -\frac{4}{3}\pi k^2 (k \cosh k - \sinh k) \hat{\mathbf{e}}_x + \frac{4}{3}i\pi k^2 (k \cosh k - \sinh k) \hat{\mathbf{e}}_y \end{cases}, \quad (\text{A4})$$

and

$$\begin{cases} \mathbf{w}_{13}^{(1)t+} = \frac{4}{3}\pi \hat{\mathbf{e}}_x + \frac{4}{3}i\pi \hat{\mathbf{e}}_y \\ \mathbf{w}_{13}^{(0)t+} = -\frac{4}{3}\pi \hat{\mathbf{e}}_z \\ \mathbf{w}_{13}^{(-1)t+} = -\frac{2}{3}\pi \hat{\mathbf{e}}_x + \frac{2}{3}i\pi \hat{\mathbf{e}}_y \end{cases}. \quad (\text{A5})$$

Similarly, the torque associated with regular basis function is obtained by

$$\begin{aligned} \mathbf{w}_{\lambda'\sigma'}^{(m)r+} &= - \int_{p.s.} (\hat{n} \cdot \bar{\bar{\sigma}}_{\lambda'm\sigma'}) \times \mathbf{r} dA = - \int_{p.v.} \nabla \cdot (\bar{\bar{\sigma}}_{\lambda'm\sigma'} \times \mathbf{r}) dV = - \int_{p.v.} (\nabla \cdot \bar{\bar{\sigma}}_{\lambda'm\sigma'}) \times \mathbf{r} dV \\ &\quad + \int_{p.v.} \bar{\bar{\sigma}}_{\lambda'm\sigma'} : \bar{\bar{\epsilon}} \cdot \bar{\bar{\mathbf{I}}} = - \int_{p.v.} (\nabla \cdot \bar{\bar{\sigma}}_{\lambda'm\sigma'}) \times \mathbf{r} dV + 0 = -i\Omega \int_{p.v.} \mathbf{v}_{\lambda'm\sigma'}^+ \times \mathbf{r} dV. \end{aligned} \quad (\text{A6})$$

Here, $\bar{\bar{\epsilon}}$ represents permutation tensor and $\bar{\bar{\mathbf{I}}}$ denotes identity tensor. The non-zero elements of torque in $\mathbf{w}_{\lambda'\sigma'}^{(m)r+}$ exist only for $\lambda' = 1$, $\sigma' = 1$:

$$\begin{cases} \mathbf{w}_{11}^{(1)r+} = \frac{8}{3}\pi [-3k \cosh k + (3 + k^2) \sinh k] \hat{\mathbf{e}}_x - \frac{8}{3}i\pi [3k \cosh k - (3 + k^2) \sinh k] \hat{\mathbf{e}}_y \\ \mathbf{w}_{11}^{(0)r+} = -\frac{8}{3}\pi [-3k \cosh k + (3 + k^2) \sinh k] \hat{\mathbf{e}}_z \\ \mathbf{w}_{11}^{(-1)r+} = \frac{4}{3}\pi [3k \cosh k - (3 + k^2) \sinh k] \hat{\mathbf{e}}_x - \frac{4}{3}i\pi [3k \cosh k - (3 + k^2) \sinh k] \hat{\mathbf{e}}_y \end{cases}. \quad (\text{A7})$$

For Stokesian dynamics, the contributions in eqs.A4, A5 and A7 are identically zero — these appear here solely due to transient fluid inertia.

Thirdly and finally, $\mathbf{w}_{\lambda\sigma}^{(m)Q-}$ means force or torque associated with singular basis function. Divergence theorem can not be applied directly for analytical extension of the fields inside

the solid volume due to the singularity at the center of the sphere. So we prefer to derive the opposite force exerted on the fluid instead of integrating inside the particle. Details are showed in the subsequent equation:

$$\begin{aligned} \mathbf{w}_{\lambda\sigma}^{(m)t-} &= \int_{p.s.} \hat{n} \cdot \bar{\sigma}_{\lambda'm\sigma'} dA = - \left(\int_{f.s.} \hat{n} \cdot \bar{\sigma}_{\lambda'm\sigma'} dA - \int_{\infty} \hat{n} \cdot \bar{\sigma}_{\lambda'm\sigma'} dA \right) \\ &= -i\Omega \int_{f.v.} \nabla \cdot \bar{\sigma}_{\lambda'm\sigma'} dV + \int_{\infty} \hat{n} \cdot \bar{\sigma}_{\lambda'm\sigma'} dA = -i\Omega \int_{f.v.} \mathbf{v}_{\lambda m\sigma}^- dV + \int_{\infty} \hat{n} \cdot \bar{\sigma}_{\lambda'm\sigma'} dA, \end{aligned} \quad (\text{A8})$$

where $\int_{\infty} \cdots dA$ is area integral at infinity, $\int_{f.s.} \cdots dA$ is area integral for liquid domain including infinity as well as solid-fluid interface, and $\int_{f.v.} \cdots dV$ is volume integral of entire fluid volume. All non-trivial elements in force $\mathbf{w}_{\lambda\sigma}^{(m)t-}$ are listed by

$$\begin{cases} \mathbf{w}_{12}^{(1)t-} = -\frac{8}{3}\pi e^{-k}(1+k)k^2 \hat{\mathbf{e}}_x - \frac{8}{3}i\pi e^{-k}(1+k)k^2 \hat{\mathbf{e}}_y \\ \mathbf{w}_{12}^{(0)t-} = \frac{8}{3}\pi e^{-k}(1+k)k^2 \hat{\mathbf{e}}_z \\ \mathbf{w}_{12}^{(-1)t-} = \frac{4}{3}\pi e^{-k}(1+k)k^2 \hat{\mathbf{e}}_x - \frac{4}{3}i\pi e^{-k}(1+k)k^2 \hat{\mathbf{e}}_y \end{cases}, \quad (\text{A9})$$

and

$$\begin{cases} \mathbf{w}_{13}^{(1)t-} = \frac{4}{3}\pi \hat{\mathbf{e}}_x + \frac{4}{3}i\pi \hat{\mathbf{e}}_y \\ \mathbf{w}_{13}^{(0)t-} = -\frac{4}{3}\pi \hat{\mathbf{e}}_z \\ \mathbf{w}_{13}^{(-1)t-} = -\frac{2}{3}\pi \hat{\mathbf{e}}_x + \frac{2}{3}i\pi \hat{\mathbf{e}}_y \end{cases}. \quad (\text{A10})$$

On the other hand, torque generated by singular basis function is obtained by the same logic as that in eqs.A6 and A8. Consequently, we find:

$$\mathbf{w}_{\lambda\sigma}^{(m)r-} = - \int_{p.s.} (\hat{n} \cdot \bar{\sigma}_{\lambda'm\sigma'}) \times \mathbf{r} dA = i\Omega \int_{f.v.} \mathbf{v}_{\lambda m\sigma}^- \times \mathbf{r} dV - \int_{\infty} (\hat{n} \cdot \bar{\sigma}_{\lambda'm\sigma'}) \times \mathbf{r} dA. \quad (\text{A11})$$

Finally, non-zero elements in torque $\mathbf{w}_{\lambda\sigma}^{(m)r-}$ are constructed as:

$$\begin{cases} \mathbf{w}_{11}^{(1)r-} = \frac{8}{3}\pi e^{-k}(3+3k+k^2) \hat{\mathbf{e}}_x + \frac{8}{3}i\pi e^{-k}(3+3k+k^2) \hat{\mathbf{e}}_y \\ \mathbf{w}_{11}^{(0)r-} = -\frac{8}{3}\pi e^{-k}(3+3k+k^2) \hat{\mathbf{e}}_z \\ \mathbf{w}_{11}^{(-1)r-} = -\frac{4}{3}\pi e^{-k}(3+3k+k^2) \hat{\mathbf{e}}_x + \frac{4}{3}i\pi e^{-k}(3+3k+k^2) \hat{\mathbf{e}}_y \end{cases}. \quad (\text{A12})$$

After all of these elements are known, the friction tensors can be constructed using eq.27.

- [1] Edward J Stancik, Anne L Hawkinson, Jan Vermant, and Gerald G Fuller. Dynamic transitions and oscillatory melting of a two-dimensional crystal subjected to shear flow. *Journal of rheology*, 48(1):159–173, 2004.

- [2] Farzad F Dizaji, Jeffrey S Marshall, and John R Grant. Collision and breakup of fractal particle agglomerates in a shear flow. *Journal of Fluid Mechanics*, 862, 2019.
- [3] J. Bławdziewicz and S. Bhattacharya. Comment on “Drift without flux: Brownian walker with a space-dependent diffusion coefficient”. *Europhys. Lett.*, 63:789–90, 2003.
- [4] John F Brady and Jeffrey F Morris. Microstructure of strongly sheared suspensions and its impact on rheology and diffusion. *Journal of Fluid Mechanics*, 348:103–139, 1997.
- [5] S Bhattacharya, DK Gurung, and S Navardi. Radial distribution and axial dispersion of suspended particles inside a narrow cylinder due to mildly inertial flow. *Physics of Fluids*, 25(3):033304, 2013.
- [6] Venkataramaiah Seshadri and SP Sutura. Concentration changes of suspensions of rigid spheres flowing through tubes. *Journal of Colloid and Interface Science*, 27(1):101–110, 1968.
- [7] Sukalyan Bhattacharya, Shahin Navardi, et al. Radial lift on a suspended finite-sized sphere due to fluid inertia for low-reynolds-number flow through a cylinder. *Journal of Fluid Mechanics*, 722:159, 2013.
- [8] Henry C Fu, Thomas R Powers, Roman Stocker, et al. Separation of microscale chiral objects by shear flow. *Physical review letters*, 102(15):158103, 2009.
- [9] Martin Frank, Douglas Anderson, Eric R Weeks, and Jeffrey F Morris. Particle migration in pressure-driven flow of a brownian suspension. *Journal of Fluid Mechanics*, 493(493):363–378, 2003.
- [10] Zhigang Li and German Drazer. Separation of suspended particles by arrays of obstacles in microfluidic devices. *Physical review letters*, 98(5):050602, 2007.
- [11] S. Navardi, S. Bhattacharya, and H. Wu. Stokesian simulation of two unequal spheres in a pressure-driven flow through a cylinder. *Computers and Fluids*, 121:145–163, 2015.
- [12] Thomas G Mason, Kavita Ganesan, J Harry van Zanten, Denis Wirtz, and Scot C Kuo. Particle tracking microrheology of complex fluids. *Physical review letters*, 79(17):3282, 1997.
- [13] Todd M Squires. Nonlinear microrheology: bulk stresses versus direct interactions. *Langmuir*, 24(4):1147–1159, 2008.
- [14] J. A. Eastman, S. U. S. Choi, S. Li, W. Yu, and L. J. Thompson. Anomalously increased effective thermal conductivities of ethylene glycol-based nanofluids containing copper nanoparticles. *Appl. Phys. Lett.*, 78:718–20, 2001.
- [15] John M Kincaid and EGD Cohen. Nano-and pico-scale transport phenomena in fluids. *Journal*

- of Statistical Physics*, 109(3):361–371, 2002.
- [16] R. B. Jones. Spherical particle in Poiseuille flow between planar walls. *J. Chem. Phys.*, 121:483–500, 2004.
- [17] B. Cichocki and R. B. Jones. Image representation of a spherical particle near a hard wall. *Physica A*, 258:273–302, 1998.
- [18] Louis J Durlofsky and John F Brady. Dynamic simulation of bounded suspensions of hydrodynamically interacting particles. *Journal of Fluid Mechanics*, 200:39–67, 1989.
- [19] S. Navardi and S. Bhattacharya. General methodology to evaluate two-particle hydrodynamic friction inside cylinder-bound viscous fluid. *Computers and Fluids*, 76:149–169, 2013.
- [20] Thanh N Phung, John F Brady, and Georges Bossis. Stokesian dynamics simulation of brownian suspensions. *Journal of Fluid Mechanics*, 313:181–207, 1996.
- [21] Ashok S Sangani and Guobiao Mo. An $O(n)$ algorithm for stokes and laplace interactions of particles. *Physics of Fluids*, 8(8):1990–2010, 1996.
- [22] A. Sierou and J. F. Brady. Accelerated Stokesian dynamics simulations. *J. Fluid Mech.*, 448:115–46, 2001.
- [23] B. U. Felderhof. Estimating the viscoelastic moduli of a complex fluid from observation of Brownian motion. *J. Chem. Phys.*, 131:ARTN:164904, 2009.
- [24] B. U. Felderhof. Estimating the viscoelastic moduli of complex fluids from observation of Brownian motion of a particle confined to a harmonic trap. *J. Chem. Phys.*, 134:ARTN:204910, 2011.
- [25] A.M. Leshansky, O.M. Lavrenteva, and A. Nir. The leading effect of fluid inertia on the motion of rigid bodies at low Reynolds number. *J. Fluid Mech.*, 505:235–248, 2004.
- [26] H. Clercx and P. Schramm. Brownian particles in shear flow and harmonic potential. *Physical Review A*, 46:1942, 1992.
- [27] H. Clercx and P. Schramm. Retarded hydrodynamic interactions in suspensions. *Physica A*, 174:325, 1991.
- [28] H. Clercx and P. Schramm. Retarded hydrodynamic interaction between two spheres immersed in a viscous incompressible fluid. *Physics of Fluids*, 31:ARTN.053604, 2019.
- [29] Bo Liu and S Bhattacharya. Vector field solution for brinkman equation in presence of disconnected spheres. *Physical Review Fluids*, 5(10):104303, 2020.
- [30] B Cichocki, BU Felderhof, and R Schmitz. Hydrodynamic interactions between two spherical

particles. *PhysicoChem. Hyd*, 10:383–403, 1988.

- [31] Raymond G Cox and Howard Brenner. The slow motion of a sphere through a viscous fluid towards a plane surface—ii small gap widths, including inertial effects. *Chemical Engineering Science*, 22(12):1753–1777, 1967.